

Lawrence Berkeley National Laboratory

Molecular Foundry

Title

Perovskite Quantum Wells Formation Mechanism for Stable Efficient Perovskite Photovoltaics—A Real-Time Phase-Transition Study

Permalink

<https://escholarship.org/uc/item/7918m62s>

Journal

Advanced Materials, 33(7)

ISSN

0935-9648

Authors

Hu, Hanlin
Qin, Minchao
Fong, Patrick WK
et al.

Publication Date

2021-02-01

DOI

10.1002/adma.202006238

Peer reviewed

Perovskite Quantum Wells Formation Mechanism for Stable Efficient Perovskite Photovoltaics—A Real-Time Phase-Transition Study

Hanlin Hu, Minchao Qin, Patrick W. K. Fong, Zhiwei Ren, Xuejuan Wan,*
Mriganka Singh, Chun-Jen Su, U-Ser Jeng, Liang Li, Jiajie Zhu, Mingjian Yuan,
Xinhui Lu, Chih-Wei Chu, and Gang Li*

The combination of a bulk 3D perovskite layer and a reduced dimensional perovskite layer (perovskite quantum wells (PQWs)) is demonstrated to enhance the performance of perovskite solar cells (PSCs) significantly in terms of stability and efficiency. This perovskite hierarchy has attracted intensive research interest; however, the in-depth formation mechanism of perovskite quantum wells on top of a 3D perovskite layer is not clearly understood and is therefore the focus of this study. Along with *ex situ* morphology and photophysical characterization, the time-resolved grazing-incidence wide-angle X-ray scattering (TS-GIWAXS) technique performed in this study provides real-time insights on the phase-transition during the organic cation (HTAB ligand molecule) coating and PQWs/3D architecture formation process. A strikingly strong ionic reaction between the 3D perovskite and the long-chain organic cation leads to the quick formation of an ordered intermediate phase within only a few seconds. The optimal PQWs/3D architecture is achieved by controlling the HTAB casting, which is assisted by time-of-flight SIMS characterization. By controlling the second ionic reaction during the long-chain cation coating process, along with the fluorinated poly(triarylamine) (PTAA) as a hole-transport layer, the perovskite solar cells demonstrate efficiencies exceeding 22% along with drastically improved device stability.


In the search for low-cost, high-efficiency solar cells, hybrid organic–inorganic perovskite solar cells (PSCs) have attracted significant research interest worldwide owing to their advantageous properties including a high light-to-electricity power conversion efficiency (PCE),^[1,2] low cost,^[3] tunable bandgap,^[4] and scalable processability.^[5,6] In the past decade, significant progress has been made in photovoltaic performance; the recently certified 25.2%^[7] PCE, in single junction PSCs, has shown performance comparable to that of crystalline silicon solar cells. Therefore, in recent years, the focus of research has significantly shifted toward the removal of commercialization roadblocks, *i.e.*, the long-term stability of devices and scaling up the fabrication process. It has been reported that in order to scale up PSCs technology, high-temperature blade coating,^[8–10] air-knife-assisted room-temperature meniscus coating,^[9,11] and spray

Prof. H. Hu
Hoffman Institute of Advanced Materials
Shenzhen Polytechnic
7098 Liuxian Boulevard, Shenzhen 518055, China

Dr. M. Qin, Prof. X. Li
Department of Physics
The Chinese University of Hong Kong
Shatin 999 077, Hong Kong

Dr. P. W. K. Fong, Dr. Z. W. Ren, Prof. G. Li
Department of Electronic and Information Engineering
Research Institute for Smart Energy (RISE)
The Hong Kong Polytechnic University
Hung Hom, Kowloon, Hong Kong
E-mail: gang.w.li@polyu.edu.hk

Prof. X. Wan
Shenzhen Key Laboratory of Polymer Science and Technology
College of Materials Science and Engineering
Shenzhen University
Shenzhen 518060, China
E-mail: wanxj@szu.edu.cn

 The ORCID identification number(s) for the author(s) of this article can be found under <https://doi.org/10.1002/adma.202006238>.

Dr. M. Singh, Prof. C.-W. Chu
Research Center for Applied Sciences
Academia Sinica
Taipei 11529, Taiwan

Dr. C.-J. Su, Dr. U.-S. Jeng
National Synchrotron Radiation Research Center
Hsinchu Science Park
Hsinchu 30 076, Taiwan

Dr. L. Li
New York University Abu Dhabi
Abu Dhabi 129188, United Arab Emirates

Dr. J. Zhu
School of Physics Science and Engineering
Tongji University
Siping Rd 1239, Shanghai 200092, China

Prof. M. Yuan
Renewable Energy Conversion and Storage Center (RECAST)
College of Chemistry
Nankai University
Tianjin 300071, China

DOI: 10.1002/adma.202006238

coating^[12,13] can be employed to fabricate high-quality perovskite solar cells with desirable photovoltaic performance. However, long-term stability under operational conditions must first be ensured.

Perovskite quantum wells (PQWs, low-dimensional perovskite or quasi-2D perovskite) exhibit drastically enhanced stability in contrast to the traditional 3D perovskite; this ability originates from the relatively long-organic-chain ligands that form the PQWs. In contrast to the smaller size cations, such as FA, MA, Cs, the ligand molecules with a relatively longer chain can form an interdigitating structure at the interface stabilized by the van der Waals force, resulting in an overall stabilization of the stacked perovskite hierarchy. Several types of aryl-ammonium and alkyl-ammonium ligands, such as butylammonium,^[14,15] phenethylammonium pentafluorophenylethylammonium,^[16,17] and hexyl-trimethylammonium^[18] etc., have been investigated and adopted for PQWs. Dou and co-workers demonstrated that the inorganic and organic building blocks of perovskite materials can be modified, yielding widely tunable single-crystalline PQWs.^[19] The perovskite lattices terminated by organic ligand molecules provide a strong resistance to water and an increased formation of energy for the perovskite quantum wells compared to their 3D perovskite counterpart. Furthermore, they can significantly suppress the migration of mobile ions within the perovskite materials. All these can synergistically act against perovskite decomposition, which is induced either by water or ion-migration, leading to significantly improved thermal and humidity stability. The photovoltaic performance of pure 2D perovskite PSCs is not at par with that of its 3D perovskite counterpart owing to the issue of anisotropic charge-carrier transport. To combine the excellent light-to-electricity efficiency of the 3D perovskite with the desired stability of the perovskite quantum wells, the hierarchy of building a low-dimensional perovskite layer on top of a 3D bulk perovskite layer has been introduced. In the last few years, perovskite solar cells based on the PQWs/3D perovskite hierarchy have been reported to demonstrate a photovoltaic performance with an efficiency exceeding 20%, comparable with that of pure 3D devices. Notably, the stacked PQWs/3D hierarchy exhibits a superior thermal stability and long-term operating stability, as compared to pure 3D devices.

Wang et al. introduced ligand molecules in a precursor solution prepared for 3D perovskite, enabling the formation of PQWs on top of the 3D perovskite bulk layer and consequently yielding the PQWs/3D perovskite hierarchy.^[20] It was also reported that casting ligand molecules on top of a 3D perovskite bulk layer via spin coating or dip coating can also lead to the formation of PQWs on top of the layer.^[14,21–25] The recently certified PCE of PSCs based on this approach has shown an efficiency of 22.7%,^[18] indicating potential benefits and applications of this perovskite hierarchy. Controlling the formation of PQWs on top of a 3D perovskite is critical for stacked PQWs/3D PSCs. Thus far, most studies on PQWs/3D perovskite have focused on the photovoltaic performance (including stability) after the formation of the hierarchy; while the critical issue of determining how the coated ligand molecules convert the 3D perovskite lattice into the reduced-dimensional perovskite structure is rarely explored. The poor understanding of the hierarchy formation mechanism leads

to the control of PQWs by empirical trial-and-error, impeding further scale-up processes and industrial implementation in the near future.

Here, we explore in detail the formation mechanism of PQWs on top of a 3D perovskite bulk layer through the real-time tracking of crystal phase evolution with the help of in situ grazing-incidence wide-angle scattering measurements (GIWAXS) conducted during the ligand molecule (hexyltrimethylammoniumbromide) coating process. Theoretically supported by the density function theory (DFT) calculation, we first reveal that there is a strong chemical reaction between the ligand molecules (ions) and the 3D perovskite layer; this results in a highly ordered intermediate adduct phase involving the ligand molecules. Upon post-thermal annealing, the adduct phase is converted into compact PQWs, as indicated by the GIWAXS measurement presenting an enlarged q value. The formation of PQWs can be controlled via a chemical reaction by tuning the amount of ligand molecules, which is reflected by the change in intensity of the characteristic scattering peaks of PQWs and 3D perovskite, combined with time-of-flight secondary-ion mass spectrometry (ToF-SIMS). By building a thin structure of PQWs on top of a 3D perovskite bulk layer, we successfully demonstrate a highly stable perovskite photoactive layer and PSCs against high humidity (70–75%). Moreover, this stacked perovskite hierarchy enables a superior thermal stability based on a new dopant-free conjugated hole transporting layer with PCE exceeding 22%. Details regarding the PQWs formation mechanism and the relative phase transformation process elucidated in this study will guide the control of chemical reactions toward the desired PQWs/3D perovskite hierarchy, facilitating further improvements in both the optoelectronic property and stability, and ultimately benefiting the implementation of PQWs modified with the 3D perovskite hierarchy in the near future.

Figure 1a,b depicts schematics of the traditional 3D and PQWs heterostructures, respectively. A traditional 3D perovskite thin film ($\text{Cs}_{0.05}\text{FA}_{0.81}\text{MA}_{0.14}\text{PbI}_{2.55}\text{Br}_{0.45}$) was obtained via the spin-coating method assisted with anti-solvent (chlorobenzene) dripping and followed by thermal annealing. To explore the formation of PQWs on top of the 3D perovskite bulk layer, a $0\text{--}100 \times 10^{-3}$ M solution of hexyltrimethylammonium bromide (HTAB) was prepared in chlorobenzene: isopropanol (9:1 by volume) mixed solvents were then spin-coated on top of the 3D perovskite surface. Next, the samples were transferred to a hotplate for post thermal annealing at 120 °C for 10 min to form the PQWs. First, atomic force microscopy (AFM) and scanning electron microscopy (SEM) was utilized to examine the morphology of the PQWs stacked perovskite thin film in comparison to the pristine one. Figure 1c–f presents a topographic AFM image of perovskite thin films after being treated with the following different concentrations of HTAB: 0, 1, 10, and 100×10^{-3} M, respectively. In contrast to the pristine perovskite film (0 mg mL^{-1}), impressive morphology changes can be observed after building PQWs atop. Especially, for the sample with a high concentration (100×10^{-3} M), the complete morphological transition from a small compact-sized domain to a fibrillar crystal structure can be observed. This fibrillar structure has also been recorded by SEM in Figure S1 in the Supporting Information. Considering the 1×10^{-3} M HTAB treated sample, the morphology changed having an increased

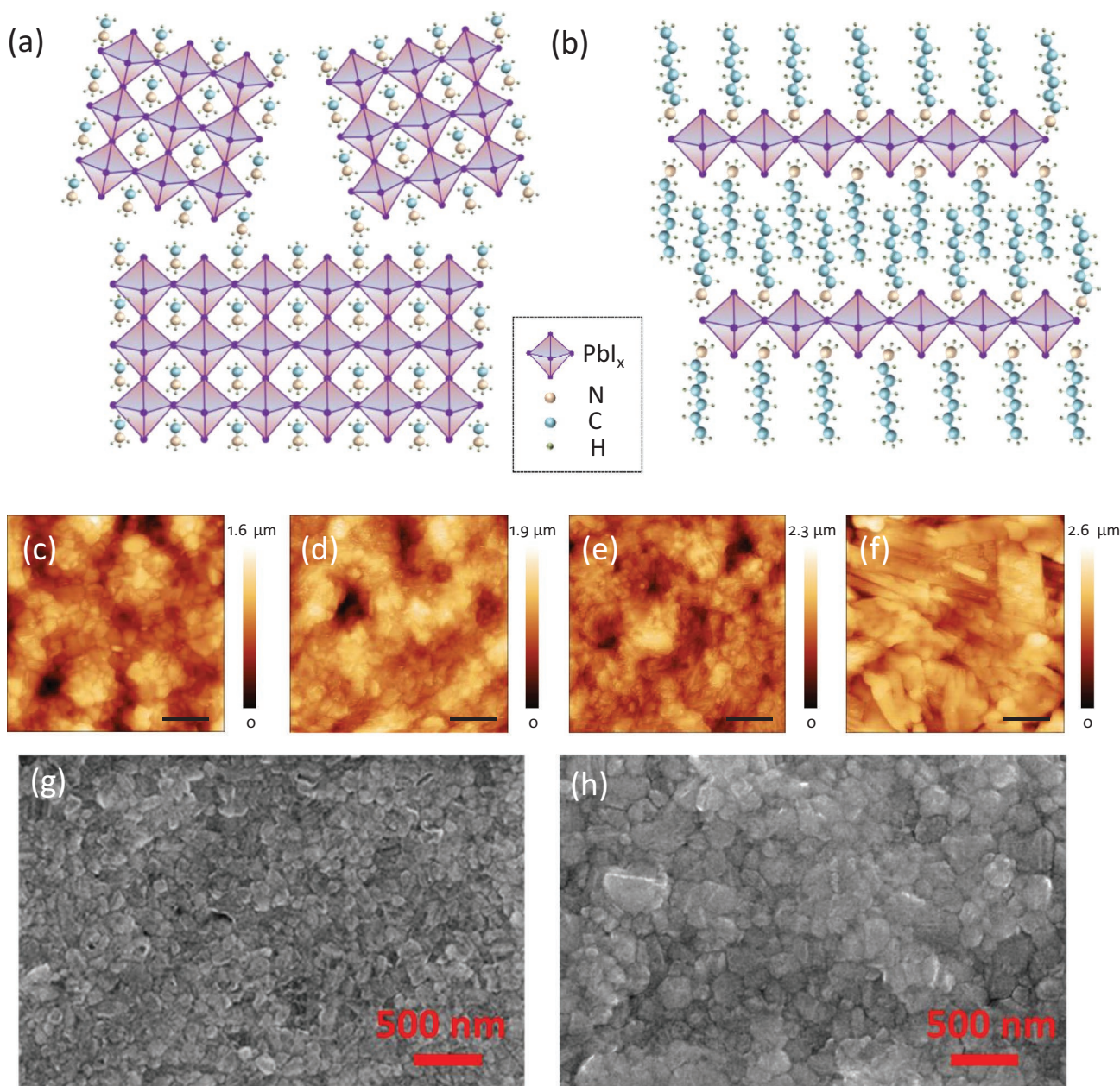


Figure 1. a,b) Schematics of a typical 3D perovskite structure (a) and a layered-perovskite structure (b) assisted by HTAB molecules. c–f) Topography AFM image of perovskite layers annealed at 120 °C for 10 min after being treated with the following concentrations of HTAB: 0, 1, 10, and 100 × 10⁻³ M, respectively. The scale bar is 1 μm. g–h) Top-view of SEM images of the perovskite layers annealed at 120 °C for 10 min after being treated with HTAB concentrations of 0 and 1 × 10⁻³ M, respectively.

grain size and a blurred grain-boundary. In addition to the topographic AFM images, it has also been demonstrated by the top-view SEM images shown in Figure 1g,h, which is similar to that of other reported studies.^[26,27]

To examine the perovskite structure after HTAB treatment, 2D GIWAXS measurement was performed on the related samples to obtain detailed information. Figure 2a–d presents the 2D GIWAXS patterns of the annealed perovskite layers at 120 °C for 10 min after being treated with different HTAB concentrations of 0, 1, 10, and 100 × 10⁻³ M respectively. For the pristine 3D perovskite sample, a strong scattering peak

located at $q = 1.0 \text{ \AA}^{-1}$ appears, which is ascribed to the (110) of 3D perovskite crystals. The broadened yielded splitting of the (110) scattering peak is due to the large size (12 mm by 12 mm) of the substrate. A detailed comparison is available in Figure S2 (Supporting Information). No scattering peak appears in the short q regime ($q < 0.9 \text{ \AA}^{-1}$), indicating a pure 3D perovskite layer. After HTAB treatment, scattering halos in the short q regime appear, as shown in Figure 2b–d, suggesting the enlarged d -spacing resulting from reduced dimensional perovskite crystals. The radial integration of the 2D GIWAXS data for perovskite samples is plotted in Figure 2e.

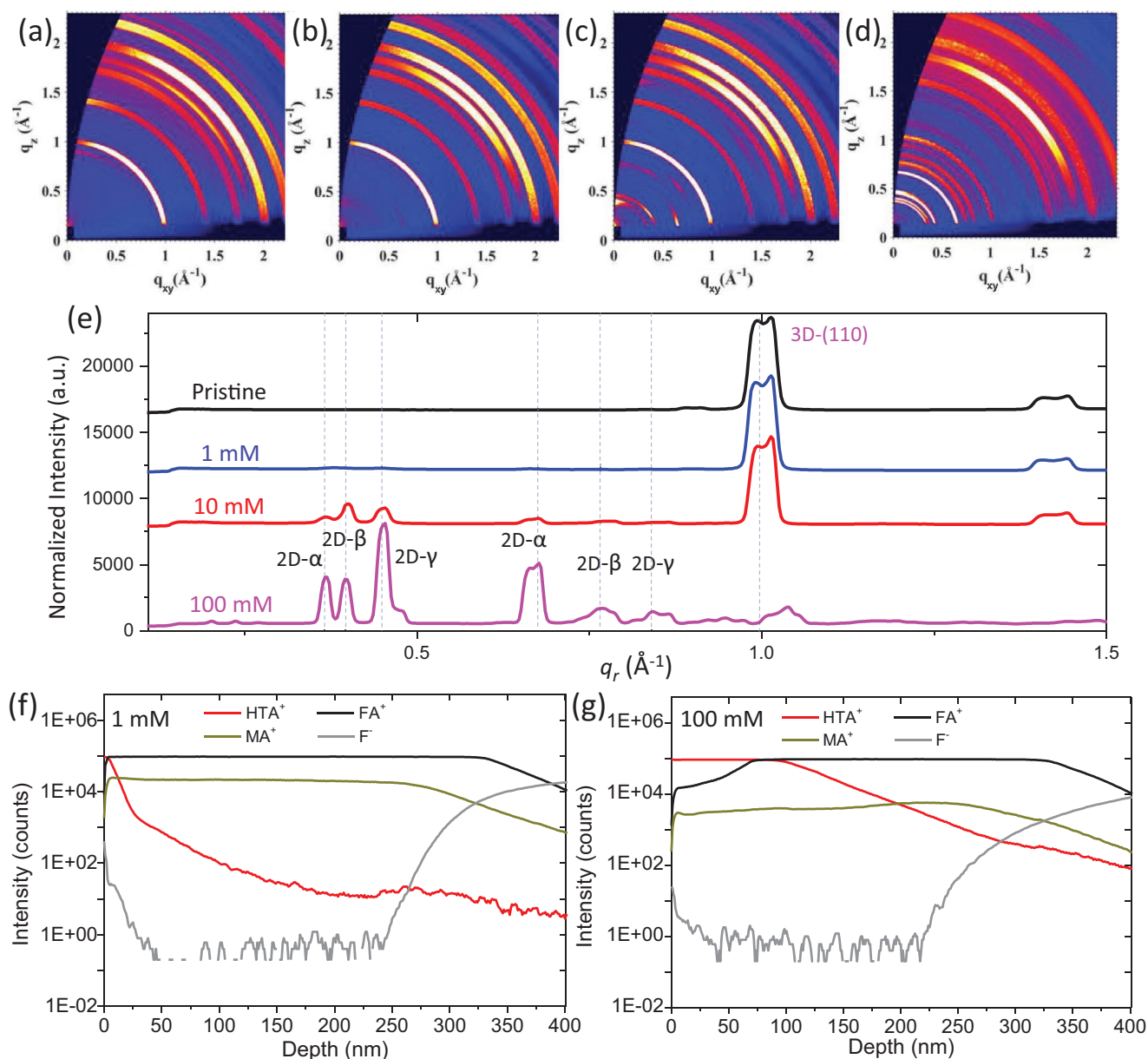


Figure 2. a–d) GIWAXS patterns of perovskite layers annealed at 120 °C for 10 min after being treated with different HTAB concentrations of 0, 1, 10, and 100×10^{-3} M, respectively. e) Radial integration of 2D GIWAXS data of annealed perovskite layers after HTAB treatment with different concentrations. f,g) TOF-SIMS depth profile of HTA⁺, FA⁺, MA⁺, and F⁻ with HTAB concentrations of 1×10^{-3} M (f) and 100×10^{-3} M (g), respectively.

The scattering features from both the 2D and 3D structures are marked by dashed lines as shown in Figure 2e. The scattering peaks with $q = 0.367, 0.396,$ and 0.451 \AA^{-1} correspond to the three different lattice d -spacings of 17.1, 15.8, and 13.9 Å, respectively. These relatively larger d -spacings resulted from the 2D structure after the inclusion of the long chain HTAB ligands. Further quantitative details can be found in the DFT calculation section. Three different structures with varying d -spacings in the 2D perovskite material have been reported in a previous study,^[28] wherein they were denoted as 2D- α , 2D- β , and 2D- γ structures, respectively. The scattering peak with $q = 1.0 \text{ \AA}^{-1}$ was attributed to the (110) of the 3D perovskite crystal structure. Along with the increasing HTAB

concentration, the following were also observed: 1) an intensified scattering intensity from the PQWs, and a decreased intensity from the 3D perovskite crystals; and 2) an increased angular distribution (mosaicity) for the scattering halos from the PQWs. In contrast to the 3D (110) scattering peak, an approximately negligible scattering peak from the PQWs was detected for the sample after the treatment of HTAB with a concentration of 1×10^{-3} M, indicating that only a very thin layer of the PQWs was formed. Impressively, the scattering peak from the 3D perovskite (110) nearly disappeared when the HTAB concentration was 100×10^{-3} M; meanwhile, strong scattering peaks from the PQWs appear. Based on the radial integration data of the GIWAXS of the perovskite samples,

we found that the formation of the 2D perovskite layer can be directly controlled by varying the concentration of HTAB, i.e., a thin PQWs layer can be obtained with a low concentration of HTAB while a thicker one can be formed with an increase in the concentration of HTAB. To gain further insight into the stacked perovskite structure, time-of-flight secondary-ion mass spectrometry (TOF-SIMS) was performed to analyze the ion depth distribution in the perovskite photo-absorber layer treated with different HTAB concentrations. The results are plotted in Figure 2g (1×10^{-3} M HTAB) and Figure 2h (100×10^{-3} M HTAB), respectively. The thickness of the perovskite layer was ≈ 400 nm according to the depth profile of F^- from the FTO substrate, which is close to the measurement performed via cross-sectional SEM, as shown in Figure S3 in the Supporting Information. As a characteristic organic spacer in PQWs, based on the depth profile of HTA^+ , it was confirmed that a thin (≈ 15 nm) PQWs layer formed on top of the 3D perovskite layer when the sample was treated by HTAB with a low concentration (1×10^{-3} M). In comparison, the measured SIMS intensity of HTA^+ nearly proceeded across the entire perovskite layer for the sample treated with a high concentration (100×10^{-3} M) of HTAB. Unlike the sample treated with a high concentration (100×10^{-3} M), the depth profiles of FA^+ and MA^+ of the sample treated with a low concentration (1×10^{-3} M) exhibited a relatively stable intensity underneath the top surface composed of PQWs. This indicated the presence of an intact 3D perovskite layer underneath

with a uniform chemical composition. A similar phenomenon was observed for other ions (I^- , Br^-), as presented in Figure S4 in the Supporting Information.

A time-resolved GIWAXS experiment was conducted to explore the in situ formation process of PQWs when HTAB was coated on top of the 3D perovskite layer. Figure 3a illustrates the time-resolved GIWAXS characterization during the HTAB dripping process on top of the 3D pristine perovskite layer. The time-resolved GIWAXS intensity map during the spin-coating of HTAB on top of the pristine 3D perovskite layer is shown in Figure 3b, and the GIWAXS intensity profiles along the q_z direction for perovskites with HTAB are plotted in Figure S5 (Supporting Information). Before the HTAB dripping process, only the scattering rings from the 3D perovskite crystals at a large q regime appear, as shown in Figure 3c. After the HTAB was coated on the 3D perovskite layer, a new ordered intermediate phase immediately emerged in the low q regime ($q = 0.31 \text{ \AA}^{-1}$), as indicated by the red arrow in Figure 3d. To further identify this species, we performed an XRD measurement on a pure HTAB sample, which presented a main diffraction peak at $2\theta = 6.13^\circ$, as shown in Figure S6 (Supporting Information), and corresponded to a d -spacing of 1.44 nm ($q = 0.436 \text{ \AA}^{-1}$).^[29] This clearly indicated that the scattering peak ($q = 0.31 \text{ \AA}^{-1}$) resulted from a new phase rather the aggregation of HTAB molecules. The detailed integrated intensity versus q corresponding to Figure 3c,d are plotted in Figure 3f. An apparent scattering peak at $q = 0.31 \text{ \AA}^{-1}$ was observed after the

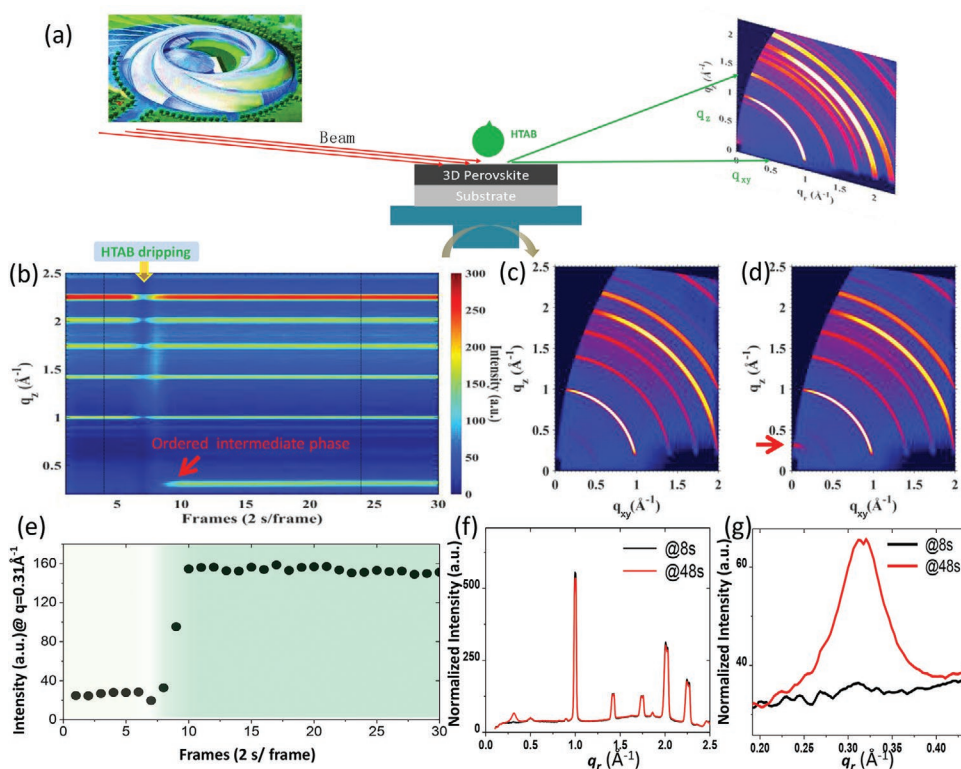


Figure 3. a) Schematic of the time-resolved GIWAXS characterization during the HTAB dripping process on top of the 3D perovskite layer. b) Time-resolved GIWAXS intensity maps showing the ordered intermediate phase formation during HTAB solution (10×10^{-3} M) spin-coating on top of the pristine 3D perovskite layer. c,d) 2D GIWAXS patterns for the perovskite films before (@8 s) and after (@48 s) HTAB dripping, as indicated by the black dashed lines in (b). e) The extracted intensity @ $q = 0.31 \text{ \AA}^{-1}$ (ordered intermediate phase, as indicated by red arrow in (d)) as a function of time. f) The integrated intensity versus q from the 2D GIWAXS patterns at 8 s (black) and 48 s (red). g) Zoom-in of the integrated intensity versus q in the low q regime.

HTAB coating, as shown in Figure 3g. To quantify the formation of this ordered intermediate phase, we plotted the intensity with $q = 0.31 \text{ \AA}^{-1}$ versus the frames (2 s per frame), as shown in Figure 3e. Surprisingly, we found that only a few seconds are needed to complete the entire formation process of the ordered intermediate phase, indicating a strong chemical reaction between the HTAB and 3D perovskite crystals. The existence of this reaction sufficiently explains the reason for the decrease in the 3D perovskite (110) scattering peak when the 2D perovskite scattering peaks in the low q regime intensified as the HTAB concentration increased. Real-time 2D GIWAXS patterns depicted in Figure S7 (Supporting Information) present the evolution of the ordered PQWs intermediate phase after HTAB treatment. To exclude the possibility that the reaction is between a residual PbI_2 and HTAB, we performed a real-time GIWAXS experiment by coating HTAB on top of a pure PbI_2 film, as shown in Figure S8 in the Supporting Information. The resulting real-time GIWAXS intensity map presents the different scattering peaks from the ordered intermediate phase in comparison to the 3D perovskite bulk layer. Moreover, a comparison of the 2D GIWAXS patterns between the perovskite and PbI_2 layers are shown in Figure S9 (Supporting Information), which indicates that the reaction is not between the residual PbI_2 and HTAB. The ordered intermediate phase eventually converted into PQWs after the thermal annealing treatment; the entire perovskite evolution process is illustrated in Figure S10 (Supporting Information).

To further examine our hypothesis, we performed the real-time GIWAXS experiment with a lower HTAB concentration ($1 \times 10^{-3} \text{ M}$) on a 3D perovskite film. As a result, the exact same location of the scattering peak in the low q regime ($q = 0.31 \text{ \AA}^{-1}$) was shown, although the intensity decreased with the same fast transition process, as expected (detailed information has been presented in Figure S11, Supporting Information). Considering the PQWs formation, we have zoomed in on the low q regime to explore the evolution process. Initially, there were no scattering signals from the pristine 3D perovskite layer (Figure 3h); then, the HTA^+ involved ordered intermediate crystal formation after the HTAB solution coating (Figure 3i); and eventually the top of the film transitioned into the 2D perovskite upon the post thermal annealing treatment, as shown in Figure 3j. In addition to the HTAB ligand molecule, other widely used ligands, namely phenethylammonium iodide (PEAI) and *tert*-butylammonium bromide (BABr) were also examined as the PQWs spacer ligands after coating the top of a 3D perovskite layer. After coating the ligand molecules on top of a 3D perovskite layer, an XRD measurement was immediately performed on the samples. New diffraction peaks at low 2θ values (larger d -spacing) appeared for both PEAi and BABr treated samples, as shown in Figure S12 in the Supporting Information. This observed phenomenon is sufficiently consistent with the HTAB results indicated above. Furthermore, there is nearly no change in the XRD spectra of the 3D perovskite film before and after the pure solvent treatment (Figure S13, Supporting Information), which excluded the solvent effect during the PQWs formation process.

The structural evolution of PQWs ($n = 1$) was investigated by first-principle calculations based on the density functional theory (see the Supporting Information for computational

details). The lattice constants of the structures of the 3D perovskite intercalated by the HTA^+ ions replacing FA^+ , a) before and b) after optimization, are indicated in Figure 4. The lattice constant after optimization was $a = b = 7.253 \text{ \AA}$ and $c = 28.95 \text{ \AA}$. It is important to note that, this lattice constant c includes two ligands from both the sides. The c axis is the right direction the ligand molecules pack along, resulting in different enlarged d -spacings as indicated by the scattering peaks in the low- q regime. The structure of the 3D perovskites was destroyed when the small cation (FA^+) was replaced with HTA^+ (Figure 4a,b), which revealed the strong chemical reactions that occurred between HTAB and 3D perovskites (instead of simple cation exchanges). This observation is in agreement with the real-time GIWAXS data, where intermediate phase formation occurred as soon as HTAB was coated. Furthermore, the HTA^+ ions were stabilized at the vertex of the $\text{PbI}_x\text{Br}_{3-x}$ octahedron with a binding energy of 6.72 eV (Figure 4c,d). The charge density difference at the interface between the $\text{PbI}_x\text{Br}_{3-x}$ octahedron and the PQWs is depicted in Figure 4e. The charge redistribution mainly occurs near the N atom in the PQWs, reflecting a strong interaction. The long chains contribute weakly to the charge transfer, which is in agreement with the weak charge carrier transport in the reduced-dimensional perovskite layer.

The UV-vis absorption spectra of the annealed perovskite layers at $120 \text{ }^\circ\text{C}$ for 10 min after being treated with different concentrations of HTAB are shown in Figure 5a. The blue-shift of the absorption shoulder of the perovskite film as the HTAB concentration increases corresponding to the wider bandgap of PQWs compared to the pristine 3D counterpart and the inclusion of bromide ions, the side product of the HTAB molecules. Figure 5b presents the PL spectra of the related perovskite films. As can be seen the PL peak location also exhibits a noticeable blueshift as the HTAB concentration increases. For the $100 \times 10^{-3} \text{ M}$ HTAB treated sample, the PL peak position significantly shifted to 701 nm in contrast to 769 nm of the pristine 3D sample; this was a result of the conversion of PQWs from the 3D perovskite and the inclusion of the bromide ions. Notably, PL peak quenching was observed for the sample with a moderate amount of HTAB treatment, suggesting a suppressed recombination due to the passivated top surface with reduced surface traps or defects. Planar n-i-p PSCs (as shown in Figure 5c) are then fabricated to examine the effect of HTA^+ -based PQWs on the photovoltaic performance of related devices. As expected, the highly concentrated HTAB-treated samples demonstrated significantly inferior photovoltaic performance, due to the 3D perovskite structure severely diminished by the HTAB. In comparison, the device treated by HTAB with a moderate concentration ($1 \times 10^{-3} \text{ M}$) yielded a PCE of up to 22.02%, which is higher than that of the pristine 3D perovskite device (20.95% champion device), as shown in Figure 5d. The enhanced PCE was mainly due to the increased V_{OC} (by 30 mV), in agreement with the reported results.^[18,26,30] The photovoltaic parameters are available in detail in Table S1 in the Supporting Information. The PCE distribution (from over 20 devices in each condition) as a function of the HTAB concentration is plotted in Figure S14 in the Supporting Information. The increased V_{OC} indicates that the PQWs with a wide bandgap effectively passivated the 3D top surface, which led to a reduced trap density and resulted in a suppressed non-radiative recombination. This was also

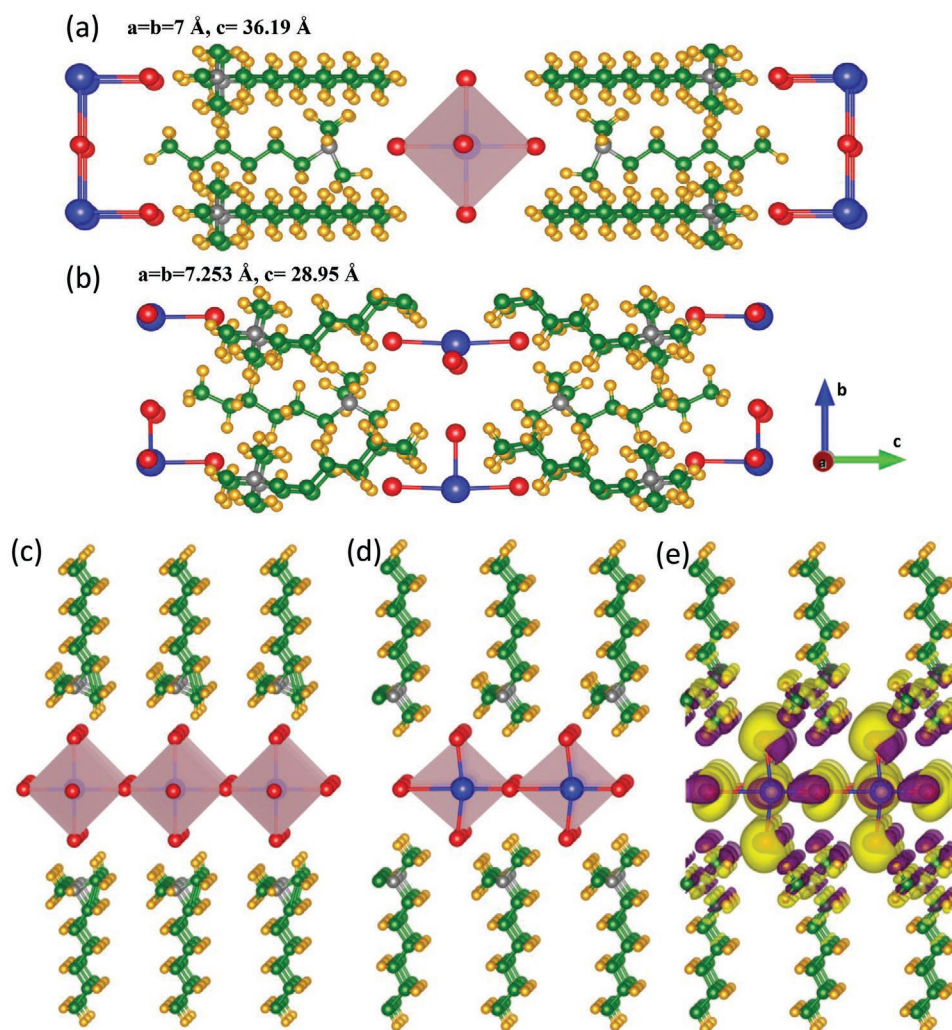


Figure 4. a,b) Structures of 3D perovskite intercalated by HTA⁺ ions to replace FA⁺ before (a) and after (b) optimization. c,d) Structures of 2D perovskite absorbed by PQWs before (c) and after (d) optimization. Charge density difference between 2D perovskite and PQWs. Yellow and purple color indicate charge accumulation and depletion, respectively. Isovalues of isosurfaces were set to 0.002 e bohr⁻³.

observed in PSCs upon poly(triarylamine) (PTAA) as a hole-transport layer (HTL), as shown in Figure S15 (Supporting Information).

The stability issue for high efficiency PSCs with a lithium salt doped Spiro-OMeTAD HTL is well-documented due to the lithium salt. PTAA is an alternative widely used HTL. In this study, dopant free PTAA was used for the fabrication of perovskite solar cells based on a 1×10^{-3} M HTAB treated perovskite, with a champion PCE of 20.09%. This value is $\approx 10\%$ lower than that in the case of the traditional salt doped Spiro-OMeTAD HTL. Through the floriation strategy modified PTAA, called 1F-PTAA (the molecular structure is available in Figure S16 in the Supporting Information), a high PCE of 22.16% was achieved (Figure 5e) with a stabilized PCE of 21.89%, as shown in Figure 5f; this is, thus far, the best among the reported perovskite solar cells with dopant free HTLs. In contrast to the benchmark material PTAA, the incorporation of fluorine atoms into the PTAA polymer chain resulted in a deeper HOMO energy level,^[31] yielding an improved energy

level matching of 1F-PTAA molecules with valance band maximums of the perovskite photoactive layer, which facilitates a more efficient charge extraction. The related energy diagrams are available in in Figure S17 in the Supporting Information. Notably, the new HTL leads to a PSC with negligible hysteresis from the forward and reverse scans, as shown in Figure S18 in the Supporting Information. The time-resolved PL (Figure 5g) confirms an over threefold increase in the charge carrier lifetime after the application of the PQWs on top of the pristine 3D perovskite bulk layer ($t = 127$ ns for pristine 3D perovskite while $t = 423$ ns for the PQWs modified one), once again suggesting the high optoelectronic quality of the 3D/PQWs perovskite film and a suppressed non-radiative recombination. The value of the integrated J_{SC} obtained from the EQE spectra (22.59 mA cm^{-2}) is in agreement with the $J-V$ measurement (23.72 mA cm^{-2}) within an error of 5%, as shown in Figure 5h.

Finally, we evaluated the influence of the 3D/PQWs heterostructure regarding the ambient and thermal stabilities.

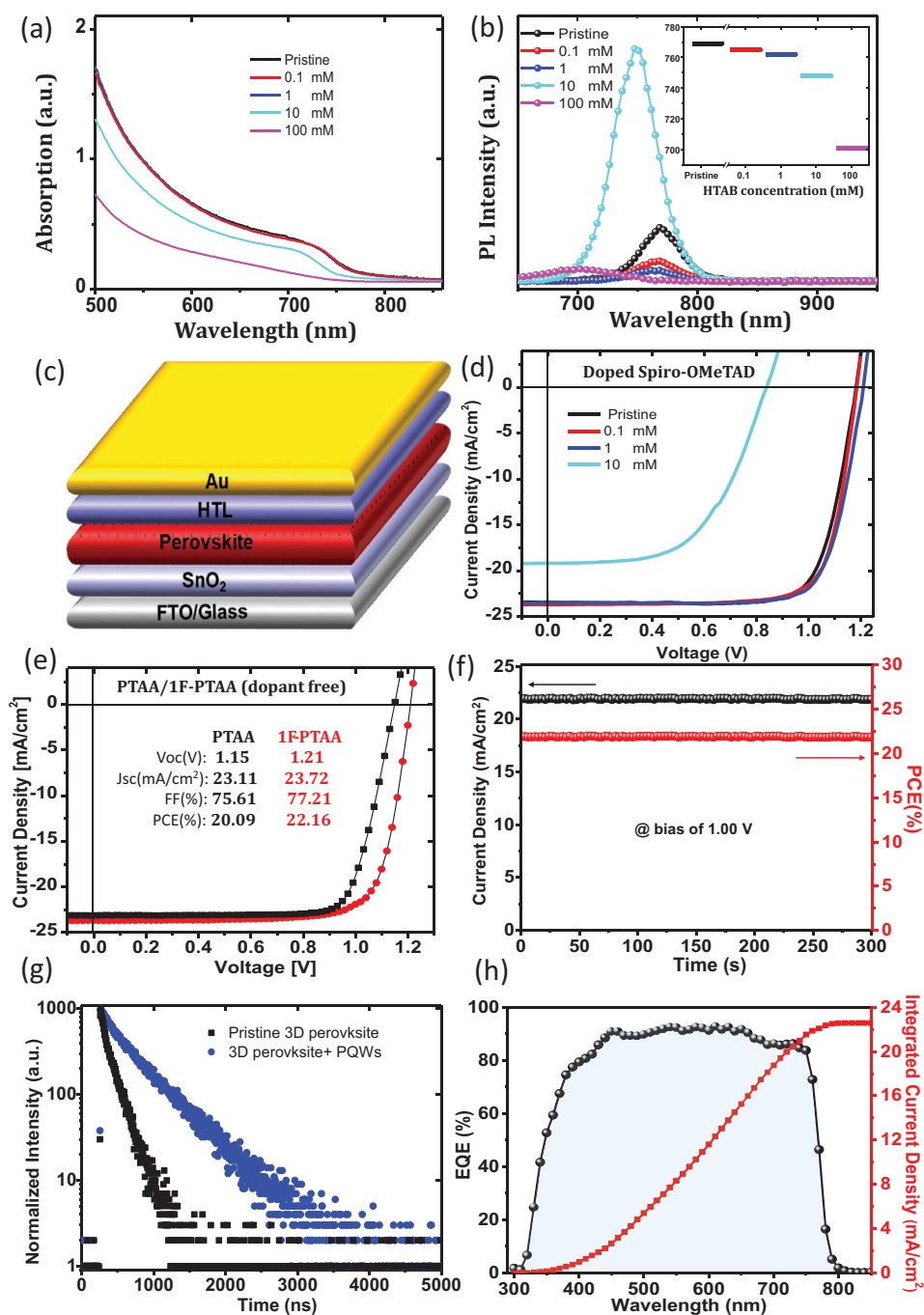


Figure 5. a,b) UV-vis absorption spectra (a) and PL spectra (b) of perovskite layers annealed at 120 °C for 10 min after being treated with HTAB with different concentrations. c) Device structure of conventional planar PSC. d) 1 sun J - V characteristic curves of planar PSCs upon doped spiro-OMeTAD with a perovskite light-absorber layer treated with HTAB with different concentrations as indicated. e) 1 sun J - V characteristic curves of planar n-i-p perovskite solar cells upon undoped PTAA/1F-PTAA with perovskite light-absorber layer treated with 1×10^{-3} M HTAB. f) Stabilized photocurrent measurement at a bias voltage of maximum power point (1.00 V) under 1 sun illumination. g) Time-resolved PL decay traces recorded from pristine perovskite film and 1×10^{-3} M HTAB treated one, excited by 470 nm. h) EQE spectrum and integrated J_{SC} for champion device upon pure 1F-PTAA.

Figure 6a presents photographs of fresh perovskite films (substrate size: 1.5 cm × 2.0 cm) treated with different HTAB concentrations, as indicated, and the respective aged ones stored in an ambient condition with an HR of 70–75% for 48 h at room temperature. Compared to the rapid decaying of the pristine sample and the highly concentrated HTAB

treated sample, the moderately concentrated HTAB treated perovskite film remained blackish in color, indicating a strong protection of PQWs against water molecules in an ambient condition. To quantify the difference in terms of ambient stability, we further evaluated the PSC photovoltaic performance with different perovskite light-harvesting

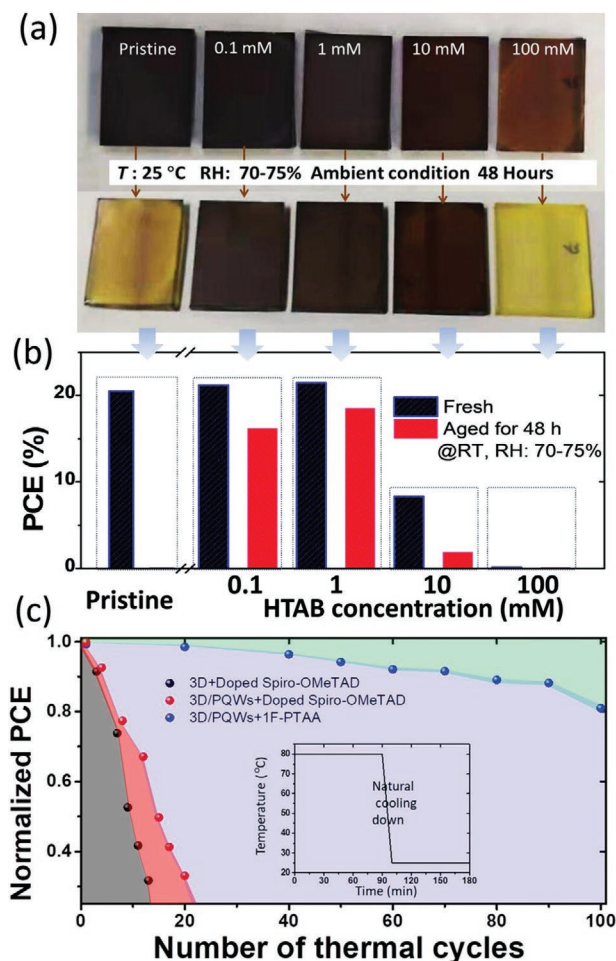


Figure 6. a) Photographs of perovskite films (substrate size: 1.5 cm \times 2.0 cm) treated with different HTAB concentrations as indicated and stored under ambient conditions at room temperature with HR of 70–75% for 48 h. b) Comparison of photovoltaic performance between the as-prepared perovskite photoactive layer treated with different HTAB concentrations and stored under ambient conditions at room temperature with HR of 70–75% for 48 h. c) Thermal stability of a normal structure of FTO/SnO₂/Cs_{0.05}FA_{0.81}MA_{0.14}PbI_{2.55}Br_{0.45}/HTL/Au (black) device tested in N₂ filled glove-box.

layers of both fresh and aged ones, by completing the HTL (Lithium salt doped Spiro-OMeTAD) and Au top electrode. The pristine sample without HTAB presents approximately no photovoltaic performance after aging at room temperature, with an HR of 70–75% for 48 h due to the fast perovskite decomposition to yellow, as shown in the photograph above, although the fresh one can yield a high PCE of >20%. It is also noted that the PSC with the highly concentrated (100 \times 10⁻³ M) HTAB treated perovskite film failed to exhibit a photovoltaic performance due to the destruction of the 3D perovskite structure by the excessively long chain ions of HTA⁺. Furthermore, the one treated with a moderate concentration (1 \times 10⁻³ M) of HTAB exhibited a significantly enhanced stability in the ambient condition while yielding a decent PCE of 18.5% after 48 h of aging at an HR of 70–75%, as shown in Figure 6b, i.e., 86.0% of its initial PCE was maintained. It is a direct evidence of the significantly

enhanced stability due to the formed PQWs. We also performed a related aging test under ambient conditions, as shown in Figure S19 (Supporting Information).

Additionally, we performed a thermal stability analysis of the PQW-modified perovskite solar cells. To exclude other factors, the thermal stability tests of unencapsulated devices were conducted in an N₂-filled glove-box. We conducted a thermal cycling test (one thermal cycle: heating a device in a glove-box at 80 °C for 90 min and then natural cooling it down to room temperature for another 90 min) for the devices with the normal structure. Rapid degradation of the pristine normal perovskite device with Li-salt doped spiro-MeOTAD was observed under the thermal cycle test, while a slight improvement was observed for the PQWs modified, as shown in Figure 6c. For the PQW-modified perovskite architecture, replacing the doped spiro-OMeTAD with pure 1F-PTAA as HTL led to a significant enhancement in its thermal stability. As a result, it was able to maintain 81.0% of the initial PCE value despite undergoing 100 thermal cycles, indicating that the doped spiro-OMeTAD is the primary reason responsible for the thermal instability of the normal perovskite structure.^[32] The enhanced thermal stability for the PQW-modified perovskite architecture with pure 1F-PTAA was attributed to the synergy between suppressed ion migration by PQWs and the stable dopant-free 1F-PTAA as HTL.

We explored the in-depth mechanism of PQWs formation in the PQWs/3D heterostructure in order to realize efficient and stable perovskite solar cells. We concluded that PQWs derived from the reaction between HTAB cation molecules and 3D perovskite bulk material leads to an enlarged domain size. Time-resolved GIWAXS revealed a rapid ionic reaction immediately after HTAB casting, yielding a highly ordered intermediate phase within only a few seconds. We reported a systematic investigation on the effect of HTAB casting influencing the PQWs, morphology, photovoltaic performance, as well as the stability of the related perovskite devices. Controlling the reaction of HTAB and 3D perovskite bulk material was determined to be the primary challenge in the formation of the desired PQWs/3D perovskite hierarchy; PQWs with a thickness of \approx 15 nm on top of a 3D perovskite were obtained with a moderate concentration of HTAB (1 \times 10⁻³ M) casting. This optimal PQWs/3D perovskite hierarchy lead to an improved photovoltaic performance. More importantly, it enabled the formation of the dopant-free PTAA-derivative (1F-PTAA) with a PCE of up to 22.16%, along with significantly improved moisture and thermal stress stability.

Experimental Section

Materials: FTO glass substrates with a sheet resistance of \approx 14 Ω sq⁻¹ were purchased from OPVTECH Inc. Formamidinium Iodide (FAI) and methylammonium bromide (MABr) were supplied from Dyesol. PbBr₂ (99.99%), bis (trifluoromethane) sulfoniimide lithium salt (Li-TFSI, 99%), 4-*tert*-butylpyridine (tBP, 96%) and CsI (99.99%) were supplied from Sigma-Aldrich. Tin (II) chloride dehydrate (SnCl₂·2H₂O), thiourea, DMF, DMSO, CB, acetonitrile and were purchased from Sigma-Aldrich. PbI₂ (99.8%) were purchased from TCI. Spiro-OMeTAD (purity: 99.5%) was purchased from Feiming Science and Technology Co., Ltd. All chemicals were used as received without further treatment.

Fabrication of Devices: The PSCs were fabricated on cleaned FTO substrates. FTO substrates were sequentially rinsed by sonication in

detergent, deionized (DI) water, acetone and ethanol, and finally dried in air by nitrogen flow. Prior to the deposition of ETLs, FTO substrates were exposed to UV–ozone for 20 min. A bright yellow colloidal SnO₂ solution was synthesized by dissolving SnCl₂·2H₂O (900 mg) and thiourea (300 mg) with a molar ratio of 1:1 into 30 mL deionized water under vigorous magnetic stirring. The obtained SnO₂ colloid precursor was spin coated onto FTO substrates with a spin rate of 4000 rpm for 30 s as ETLs, and then were annealed in air at 150 °C for 20 min, then 180 °C for 20 min, and 200 °C for 1 h. Then, a second commercially available SnO₂ nanoparticles layer^[11] was spin coated with a spin rate of 4000 rpm for 30 s, followed by a thermal annealing process at 150 °C for 60 min. The Cs_{0.05}FA_{0.81}MA_{0.14}PbI_{2.55}Br_{0.45} precursor solution (1.1 M) was prepared in a mixed solvent of DMF and DMSO (4:1, v/v) in nitrogen-filled glove-box. The dissolved solution was filtered with the filter (0.45 μm, Oriental Chemicals). The perovskite precursor solution was spin-coated on ETL coated substrates following 2 steps: 1000 rpm for 10 s, 6000 rpm for 25 s. During the spin coating process, 150 μL of CB was drop-cast on perovskite precursor wet film at 15 s. Thereafter, the as-cast films were thermal annealed at 150 °C for 60 min. Filtered spiro-OMeTAD solution (80 mg dissolved in 1 mL chlorobenzene) with 29 μL of tBP and 17.5 μL of Li-TFSI (520 mg mL⁻¹ in acetonitrile) was spin coated on the top of the perovskite layer at 4000 rpm for 60 s in a glove box after the substrates cooling down to room temperature. PTAA/1F-PTAA was spin-coated from CB (6 mg mL⁻¹) with spin rate of 3000 rpm for 60 s.

The samples were then kept in a closed dark tube with oxygen flow for 24 h.^[33] Finally, 90–100 nm of gold was deposited by thermal evaporation on top of HTL layer to complete the device, using a shadow mask to pattern the electrodes. The active area of the cells was 0.09 cm², which was defined by the overlapped area of the Au electrode and the FTO stripe.

In Situ GIWAXS Measurements: In situ GIWAXS measurements were performed at the 23A small- and wide-angle X-ray scattering (SWAXS) beamline at the National Synchrotron Radiation Research Center (NSRRC), Hsinchu, Taiwan. The wavelength of X-ray was 0.124 nm (10 keV) and the scattering signals were recorded by a C9728DK area detector. The distance from the sample to detector was ≈166 mm, calibrated with a lanthanum hexaboride (LaB6) sample. The incidence angle was set at 2° to enhance the signal resolution with each frame exposure time of 2 s. The spin-coating process was carried in an air-tight chamber under N₂ atmosphere by N₂ flow, consisting of a spin-coater and a motorized syringe for remote injection of HTAB ligands. After spinning starts with 3D perovskite sample, GIWAXS measurement could start simultaneously, followed by a programmed HTAB solution injection onto the spinning film at a designated timing during the whole spinning process.

Characterization: The *J*–*V* characteristics of the devices were measured using a B1500 A semiconductor parameter analyzer under the calibrated ABET Technologies SUN 2000 solar simulator equipped with an AM 1.5 filter at 100 mW cm⁻².

The corresponding IPCE spectrum was measured in air by a QE-R3011 system from Enli Technology Co. Ltd. (Enli).

The morphologies of PSCs were investigated by a high-resolution field-emission SEM (JEOL JSM-6335F). The surface analysis for the samples was carried out by AFM “Agilent 5400 SPM”.

XRD patterns were determined by using a Rigaku SmartLab X-ray diffractometer with Cu Kα radiation.

The PL spectrum and TRPL signals of perovskite film were recorded by using Edinburgh FLSP920 spectrophotometer equipped with the excitation source of 485 nm picosecond pulsed diode laser.

Computational Method: All the calculations are performed in the framework of the density functional theory with the projector augmented plane-wave method, as implemented in the Vienna Ab initio Simulation Package (VASP).^[34] The generalized gradient approximation proposed by Perdew, Burke, and Ernzerhof is selected for the exchange–correlation potential.^[35] The cut-off energy for plane wave is set to 400 eV. The energy criterion is set to 10⁻⁵ eV in iterative solution of the Kohn–Sham equation. The Brillouin zone integration is performed at the Gamma point. All the structures are relaxed until the residual forces on the atoms have declined to less than 0.03 eV Å⁻¹.

Supporting Information

Supporting Information is available from the Wiley Online Library or from the author.

Acknowledgements

This work was financially supported by the Research Grants Council of Hong Kong (GRF grant 15246816 and CRF grant C5037-18G), The Hong Kong Polytechnic University (Project Code: 1-ZE29, 1-BBAS, and Sir Sze-yuen Chung Endowed Professorship), and Shenzhen Science and Technology Innovation Commission (Project No. JCYJ20170413154602102; JCYJ20200109105003940). The financial support from the National Natural Science Foundation of China (62004129; 21875144) and Shenzhen Polytechnic is gratefully acknowledged. X.L. thanks Research Grants Council of Hong Kong (General Research Fund No. 14314216).

Conflict of Interest

The authors declare no conflict of interest.

Keywords

perovskite photovoltaics, perovskite quantum wells, phase-transitions

Received: September 12, 2020

Revised: November 12, 2020

Published online:

- [1] M. M. Lee, J. Teuscher, T. Miyasaka, T. N. Murakami, H. J. Snaith, *Science* **2012**, *338*, 643.
- [2] H. Tan, A. Jain, O. Voznyy, X. Lan, F. P. García de Arquer, J. Z. Fan, R. Quintero-Bermudez, M. Yuan, B. Zhang, Y. Zhao, F. Fan, P. Li, L. N. Quan, Y. Zhao, Z.-H. Lu, Z. Yang, S. Hoogland, E. H. Sargent, *Science* **2017**, *355*, 722.
- [3] N. J. Jeon, J. H. Noh, W. S. Yang, Y. C. Kim, S. Ryu, J. Seo, S. Il Seok, *Nature* **2015**, *517*, 476.
- [4] H. Zhou, Q. Chen, G. Li, S. Luo, T.-b. Song, H.-S. Duan, Z. Hong, J. You, Y. Liu, Y. Yang, *Science* **2014**, *345*, 542.
- [5] Y. Deng, X. Zheng, Y. Bai, Q. Wang, J. Zhao, J. Huang, *Nat. Energy* **2018**, *3*, 560.
- [6] F. Fu, T. Feurer, T. P. Weiss, S. Pisoni, E. Avancini, C. Andres, S. Buecheler, A. N. Tiwari, *Nat. Energy* **2017**, *2*, 16190.
- [7] National Renewable Energy Laboratory solar cell efficiency chart, <http://www.nrel.gov/pv/assets/images/efficiency-chart.png>, (accessed: August 2020).
- [8] M. He, B. Li, X. Cui, B. Jiang, Y. He, Y. Chen, D. O’Neil, P. Szymanski, M. A. El-Sayed, J. Huang, Z. Lin, *Nat. Commun.* **2017**, *8*, 16045.
- [9] L.-L. Gao, C.-X. Li, C.-J. Li, G.-J. Yang, *J. Mater. Chem. A* **2017**, *5*, 1548.
- [10] Y. Fan, J. Fang, X. Chang, M.-C. Tang, D. Barrit, Z. Xu, Z. Jiang, J. Wen, H. Zhao, T. Niu, D.-M. Smilgies, S. Jin, Z. Liu, E. Q. Li, A. Amassian, S. (F.) Liu, K. Zhao, *Joule* **2019**, *3*, 2485.
- [11] H. Hu, Z. Ren, P. W. K. Fong, M. Qin, D. Liu, D. Lei, X. Lu, G. Li, *Adv. Funct. Mater.* **2019**, *29*, 1900092.
- [12] J. G. Tait, S. Manghooli, W. Qiu, L. Rakocevic, L. Kootstra, M. Jaysankar, C. A. Masse de la Huerta, U. W. Paetzold, R. Gehlhaar, D. Cheyng, P. Heremans, J. Poortmans, *J. Mater. Chem. A* **2016**, *4*, 3792.
- [13] J. H. Heo, M. H. Lee, M. H. Jang, S. H. Im, *J. Mater. Chem. A* **2016**, *4*, 17636.

- [14] D. H. Cao, C. C. Stoumpos, O. K. Farha, J. T. Hupp, M. G. Kanatzidis, *J. Am. Chem. Soc.* **2015**, *137*, 7843.
- [15] H. Tsai, W. Nie, J.-C. Blancon, C. C. Stoumpos, R. Asadpour, B. Harutyunyan, A. J. Neukirch, R. Verduzco, J. J. Crochet, S. Tretiak, L. Pedesseau, J. Even, M. A. Alam, G. Gupta, J. Lou, P. M. Ajayan, M. J. Bedzyk, M. G. Kanatzidis, A. D. Mohite, *Nature* **2016**, *536*, 312.
- [16] Y. Bai, S. Xiao, C. Hu, T. Zhang, X. Meng, H. Lin, Y. Yang, S. Yang, *Adv. Energy Mater.* **2017**, *7*, 1701038.
- [17] K. T. Cho, G. Grancini, Y. Lee, E. Oveisi, J. Ryu, O. Almora, M. Tschumi, P. A. Schouwink, G. Seo, S. Heo, J. Park, J. Jang, S. Paek, G. Garcia-Belmonte, M. K. Nazeeruddin, *Energy Environ. Sci.* **2018**, *11*, 952.
- [18] E. H. Jung, N. J. Jeon, E. Y. Park, C. S. Moon, T. J. Shin, T.-Y. Yang, J. H. Noh, J. Seo, *Nature* **2019**, *567*, 511.
- [19] Y. Gao, E. Shi, S. Deng, S. B. Shiring, J. M. Snaider, C. Liang, B. Yuan, R. Song, S. M. Janke, A. Liebman-Peláez, P. Yoo, M. Zeller, B. W. Boudouris, P. Liao, C. Zhu, V. Blum, Y. Yu, B. M. Savoie, L. Huang, L. Dou, *Nat. Chem.* **2019**, *11*, 1151.
- [20] Z. Wang, Q. Lin, F. P. Chmiel, N. Sakai, L. M. Herz, H. J. Snaith, *Nat. Energy* **2017**, *2*, 17135.
- [21] Z. Liu, K. Meng, X. Wang, Z. Qiao, Q. Xu, S. Li, L. Cheng, Z. Li, G. Chen, *Nano Lett.* **2020**, *20*, 1296.
- [22] J. Rodríguez-Romero, J. Sanchez-Diaz, C. Echeverría-Arrondo, S. Masi, D. Esparza, E. M. Barea, I. Mora-Seró, *ACS Energy Lett.* **2020**, *5*, 1013.
- [23] B.-E. Cohen, M. Wierzbowska, L. Etgar, *Adv. Funct. Mater.* **2017**, *27*, 1604733.
- [24] T. M. Koh, V. Shanmugam, J. Schlipf, L. Oesinghaus, P. Müller-Buschbaum, N. Ramakrishnan, V. Swamy, N. Mathews, P. P. Boix, S. G. Mhaisalkar, *Adv. Mater.* **2016**, *28*, 3653.
- [25] I. C. Smith, E. T. Hoke, D. Solis-Ibarra, M. D. McGehee, H. I. Karunadasa, *Angew. Chem., Int. Ed.* **2014**, *53*, 11232.
- [26] N. D. Pham, V. T. Tjong, D. Yao, W. Martens, A. Guerrero, J. Bisquert, H. Wang, *Nano Energy* **2017**, *41*, 476.
- [27] A. D. Jodlowski, C. Roldán-Carmona, G. Grancini, M. Salado, M. Ralaierisoa, S. Ahmad, N. Koch, L. Camacho, G. de Miguel, M. K. Nazeeruddin, *Nat. Energy* **2017**, *2*, 972.
- [28] Y. Liu, S. Akin, L. Pan, R. Uchida, N. Arora, J. V. Milić, A. Hinderhofer, F. Schreiber, A. R. Uhl, S. M. Zakeeruddin, A. Hagfeldt, M. I. Dar, M. Grätzel, *Sci. Adv.* **2019**, *5*, eaaw2543.
- [29] Q. Jiang, Y. Zhao, X. Zhang, X. Yang, Y. Chen, Z. Chu, Q. Ye, X. Li, Z. Yin, J. You, *Nat. Photonics* **2019**, *13*, 460.
- [30] A. H. Proppe, M. Wei, B. Chen, R. Quintero-Bermudez, S. O. Kelley, E. H. Sargent, *J. Am. Chem. Soc.* **2019**, *141*, 14180.
- [31] Y. Kim, E. H. Jung, G. Kim, D. Kim, B. J. Kim, J. Seo, *Adv. Energy Mater.* **2018**, *8*, 1801668.
- [32] X. Zhao, H.-S. Kim, J.-Y. Seo, N.-G. Park, *ACS Appl. Mater. Interfaces* **2017**, *9*, 7148.
- [33] A. Ng, Z. Ren, H. Hu, P. W. K. Fong, Q. Shen, S. H. Cheung, P. Qin, J.-W. Lee, A. B. Djurišić, S. K. So, G. Li, Y. Yang, C. Surya, *Adv. Mater.* **2018**, *30*, 1804402.
- [34] G. Kresse, D. Joubert, *Phys. Rev. B* **1999**, *59*, 1758.
- [35] J. P. Perdew, K. Burke, M. Ernzerhof, *Phys. Rev. Lett.* **1996**, *77*, 3865.